International Journal of Heat and Mass Transfer 208 (2023) 124050

Contents lists available at ScienceDirect

International Journal of Heat and Mass Transfer

journal homepage: www.elsevier.com/locate/hmt

Effect of forced convection on the formation of the as-cast structure and macrosegregation of Sn-10wt.% Pb alloy: A numerical study

Zhao Zhang, Menghuai Wu*, Haijie Zhang, Andreas Ludwig, Abdellah Kharicha

Department of Metallurgy, Chair of Simulation and Modelling of Metallurgical Processes, University of Leoben, Leoben A-8700, Austria

ARTICLE INFO

Article history:
Received 14 October 2022
Revised 20 February 2023
Accepted 1 March 2023

Keywords:
Traveling magnetic field (TMF)
Fragmentation
Remelting
Macrosegregation
As-cast structure

ABSTRACT

A series of solidification benchmark experiments based on Sn-10wt.% Pb alloy were performed at the SIMAP Laboratory in Grenoble, France (Hachani et al., 2015) to study the effect of different types of forced convection on the as-cast structure and macrosegregation. Forced convection was achieved by using a traveling magnetic field (TMF). Four cases were investigated: without TMF; TMF in the same direction as natural convection; TMF in the opposite direction as natural convection; and TMF periodically reversed with respect to natural convection. In the current study, a three-phase mixed columnar-equiaxed solidification model was used to "reproduce" the above experiments to understand the flow effect on the as-cast structure formation. The dendrite fragmentation is regarded as the only source of equiaxed grains. Remelting/destruction of equiaxed grains in the superheated melt is considered. The continuous growth of the surviving equiaxed grains and further competition with the as-developed columnar dendrites, leading to columnar-to-equiaxed transition (CET), are included. Except for Case III (i.e., a TMF in the opposite direction as natural convection), satisfactory simulation-experiment agreements in terms of the temperature field, as-cast structure and macrosegregation are obtained for the remaining three cases. Based on the simulation results, it is found that 1) TMF plays an important role in homogenizing the temperature field and promoting the formation of equiaxed grains via fragmentation, consequently facilitating the appearance of CET; 2) TMF tends to generally intensify macrosegregation and increase the number of channel segregations; and 3) the simultaneous solidification/remelting process represents a significant species/energy transport mechanism. Ignoring the remelting of equiaxed grains would lead to an overestimate of the local temperature in the remelting zone. The reason for the mismatch between the simulation and experimental results obtained for Case III is discussed.

1. Introduction

The electromagnetic field (EMF) has been widely used during the casting process because of its multiple benefits for improving the casting quality: the well-controlled flow field, the homogenization of the temperature/solute field, the promotion of grain nucleation and dendrite fragmentation, the extension of the equiaxed structure and the improvement of the segregation intensity, etc. [1–3]. One typical EMF, i.e., the traveling magnetic field (TMF), which can produce a Lorentz force in one direction, is often used to control the flow pattern (forming the so-called "butterfly" type of flow) and grain structure both in slab continuous casting processes [4–8] and laboratory experiments [9–10].

Various experiments have been performed to investigate the solidification of pure tin and its alloys, e.g., tin-lead (Sn-3 wt.% Pb, Sn-5 wt.% Pb, Pb-48 wt.% Sn) and tin-zinc (Sn-5 wt.% Zn), on the laboratory scale in a rectangular cavity under natural convection [11–17]. The experimental results show that the channel segregations are intensified with increasing cooling rate and initial solute concentration. To investigate the effect of forced convection on the as-cast structure and macrosegregation, similar experiments were performed under TMF conditions [18–21]. Specifically, Hachani et al. [20] performed a series of experiments to study the effect of different types of forced convection on the as-cast structure and macrosegregation. Forced convection was achieved by using the TMF. Four different solidification experiments based on Sn-10wt.%Pb alloy were investigated: without TMF (Case I); TMF in the same direction as natural convection (Case II); TMF in the opposite direction as natural convection (Case III); and TMF periodically reversed with respect to natural convection (Case IV).

* Corresponding author.
E-mail address: menghuai.wu@unileoben.ac.at (M. Wu).

https://doi.org/10.1016/j.ijheatmasstransfer.2023.124050

The temperature field, as-cast structure, and solute distribution of the four cases were analyzed comprehensively, which provided an excellent reference case to validate the simulation model.

Many numerical studies [22–35] have attempted to "reproduce" the above benchmark experiments [11,15,17,20]. A cellular automaton-finite element (CA-FE) solidification model [22–23] was used to simulate the solidification of the benchmark experiment [15]. Satisfactory agreement of the grain morphology was obtained, but the segregation channels could not be predicted. Two-phase volume-averaged (VA) numerical models [24–32] were also used to simulate the benchmark [11,17]. The segregation channels were excellently reproduced, but because the second solid phase, the equiaxed grains, were ignored, the credibility of the calculation results was weakened. Direct application of the two-phase VA numerical model to the cases under a TMF, makes it more difficult to "reproduce" the as-cast structure and segregation profiles [33–34]. Recently, a three-phase mixed-columnar-equiaxed VA model [35–36] was used to model benchmark Case I of Hachani et al. [20]. The numerical simulation results proved that the motion of equiaxed grains significantly affects the final distribution of the equiaxed grains and macrosegregation profiles. However, both of them ignored the remelting/destruction phenomenon occurred during the casting process. Additionally, compared to benchmark Case I, the cases under the TMF are of high interest and significance, but the simulations raise more challenges under forced convection conditions.

This study continues the work of the current authors [36–37] by including the effect of the TMF. The three-phase mixed columnar-equiaxed solidification model was extended with improved approaches for remelting and grain destruction. The extended model was used to "reproduce" the four cases of Hachani's benchmark experiments [20]. On this basis, this study focuses on explaining the formation mechanism for the as-cast structure and macrosegregation under the effect of TMFs.

2. Model description

A three-phase mixed columnar-equiaxed solidification model [38–41] was used to investigate the formation of the as-cast structure and macrosegregation of Sn-10wt.% Pb alloy in an experimental benchmark under forced convection conditions [20]. The governing equations for the model have been presented in detail elsewhere [38,41]. Three phases are considered: liquid melt (ℓ), equiaxed grains (e) and columnar dendrites (c). Their volume fractions (f_ℓ, f_e, f_c) sum up to one. Both the liquid melt and equiaxed grains are treated as moving phases, for which the corresponding Navier–Stokes equations are solved to obtain the liquid velocity ($\vec{u}_\ell$) and equiaxed velocity ($\vec{u}_e$). The columnar dendrites are assumed to be composed of a rigid phase, for which the velocity is zero ($\vec{u}_c \equiv 0$). Simple morphologies are assumed for the two solid phases: stepwise cylinders for columnar trunks and spheres for equiaxed grains. To address the drag force and other hydrodynamic interactions between phases, a dendritic envelope (f_e^{env}) is considered for equiaxed grains. The volume ratio of the solid 'dendrite' to the dendritic envelop is defined as f_{si} ($= f_e/f_e^{env}$), which was set as a constant in this study. A diffusion-governed growth kinetic is considered to treat the solidification for both solid phases. The difference between the equilibrium and volume-averaged liquid concentrations ($c_\ell^* - c_\ell$) served as the driving force for solidification. The position of the columnar tip front was traced dynamically based on the Lipton-Glicksman-Kurz (LGK) model [42]. A so-called effective equiaxed viscosity (μ_e), which increases with f_e^{env}, was used to model the interaction between the equiaxed grains [43]. When f_e^{env} reached a packing limit $f_{e,\text{packing}}$, a rigid network of equiaxed grains was built. Additionally, the equiaxed grains were captured by the columnar dendrites and fixed there when the local volume fraction of the columnar phase $f_c \geq 0.2$. Solidification shrinkage was ignored. Both thermal-solutal convection and grain sedimentation were modeled using the Boussinesq approach. The volume-averaged concentrations for each phase, i.e., c_ℓ, c_e, and c_c, were calculated. The macrosegregation was characterized by the segregation index: $c_{\text{mix}}^{\text{index}} = (c_{\text{mix}} - c_0) \times 100/c_0$, in which c_0 is the initial concentration and c_{mix} is the mixture concentration with $c_{\text{mix}} = (f_\ell\rho_\ell c_\ell + f_e\rho_e c_e + f_c\rho_c c_c)/(f_\ell\rho_\ell + f_e\rho_e + f_c\rho_c)$, where ρ_ℓ, ρ_e, ρ_c are the densities for each phase. Some important relevant modeling features for the current benchmark are described below.

2.1. Dendrite fragmentation

Dendrite fragmentation [44] is considered as the only source of equiaxed grains. The net mass transfer rate from the columnar dendrites to the equiaxed grains due to fragmentation can be calculated using

$$M_{ce} = -\gamma \cdot \left(\vec{u}_\ell - \vec{u}_c\right) \cdot \nabla c_\ell \cdot \rho_e, \tag{1}$$

where γ is the fragmentation coefficient and ∇c_ℓ is the liquid concentration gradient. All other contributions to fragmentation, e.g., the curvature effect of the dendrites, latent heat-induced thermal fluctuation, and diffusion in the interdendritic melt, are included in the single fragmentation coefficient γ. The production rate of the number density of fragments is calculated via

$$N_{ce} = \frac{M_{ce}}{\rho_e \cdot \frac{\pi}{6}\left(d_{e,\text{frag}}^0\right)^3}, \tag{2}$$

where $d_{e,\text{frag}}^0 (= \lambda_2 \cdot f_c)$ is the initial diameter of the fragment and λ_2 is the secondary dendrite arm spacing, which must be determined experimentally. Heterogeneous nucleation is ignored here.

2.2. Solidification and remelting/destruction of equiaxed grains

The solidification and remelting of equiaxed grains are treated as two asymmetric processes [45], i.e., the remelting process is not simply "inverse solidification". Schematics of the solute partitioning at the liquid–solid interface and the solute distribution in the liquid and solid during solidification and remelting processes are shown in Fig. 1.

(1) *Solidification*: the growth of the equiaxed grains is governed by diffusion. The net mass transfer rate between the liquid melt and the equiaxed grains during the solidification process is described as

$$M_{\ell e} = v_R \cdot \left(n_{eq}\pi d_e^2\right) \cdot \rho_e \cdot f_\ell, \tag{3}$$

where n_{eq} is the number density of equiaxed grains, d_e is the grain diameter, and v_R is the growth speed of equiaxed grains, which yields

$$v_R = \frac{D_\ell}{l_\ell} \cdot \frac{(c_\ell^* - c_\ell)}{\left(c_\ell^* - c_e^*\right)}, \tag{4}$$

where D_ℓ is the solute diffusion coefficient in the liquid, c_e^* is the equilibrium equiaxed concentration at the liquid/solid interface (Fig. 1(a)), and l_ℓ is the diffusion length, which is calculated using

$$l_\ell = \frac{d_e}{2}\left(1 - f_e^{\frac{1}{3}}\right). \tag{5}$$

(1) *Remelting and destruction of the equiaxed grains*: the remelting of the equiaxed grains is also governed by solute diffusion [46]. The geometrical impingement factor (f_ℓ) is unnecessary during

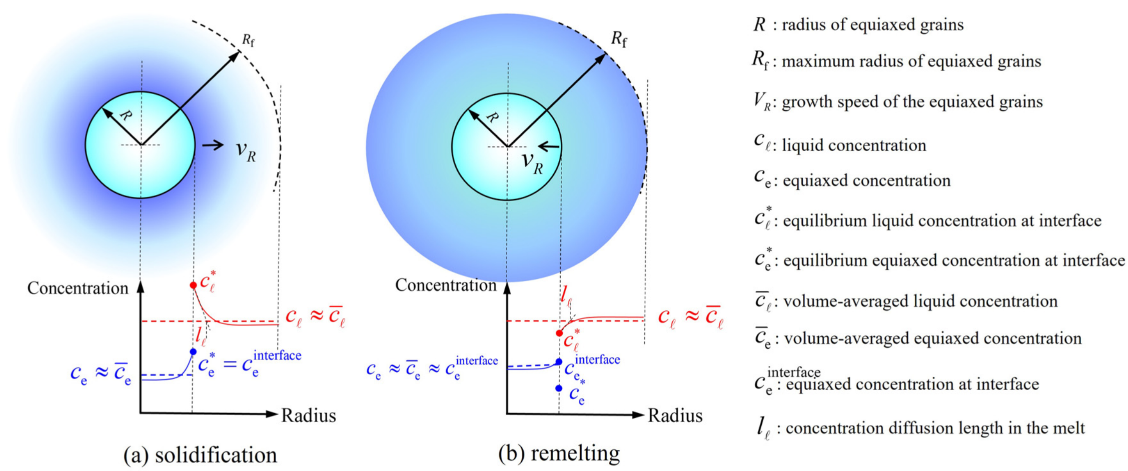

Fig. 1. Schematic of solute partitioning at the liquid–solid interface and the solute distribution in the liquid and solid: (a) solidification process; (b) remelting process.

the remelting process, and thereby, Eq. (3) is updated for the remelting process.

$$M_{\ell e} = v_R \cdot \left(n_{eq} \pi d_e^2\right) \cdot \rho_e. \tag{6}$$

Unlike the solidification process, the equilibrium concentrations (c_ℓ^* and c_e^*) are lower than the volume-averaged concentrations (c_ℓ and c_e) during the remelting process (Fig. 1(b)); thus, it is assumed that the equiaxed concentration at the liquid/solid interface ($c_e^{interface}$) is equal to c_e, and v_R is calculated using

$$v_R = \frac{D_\ell}{l_\ell} \cdot \frac{(c_\ell^* - c_\ell)}{\left(c_\ell^* - c_e\right)}. \tag{7}$$

A significant remelting process occurs when the equiaxed grains are transported into the bulk melt region, where flow might be quite turbulent. The turbulent flow effect on the remelting process is considered based on the modified diffusion length [47–48], which yields

$$l_\ell = d_e / \left(2 + 0.6 \cdot \mathrm{Sc}^{1/3} \mathrm{Re}^{1/2}\right), \tag{8}$$

where $\mathrm{Sc} = \mu / \rho_\ell D_\ell$ is the Schmidt number, $\mathrm{Re} = d_e \rho_\ell |\vec{u}_\ell - \vec{u}_e| / \mu$ is the local Reynolds number, and μ is the dynamic viscosity of the liquid melt.

To model the grain destruction, the equiaxed grains are assumed to follow a lognormal size distribution [45]. If a grain is exposed to a superheated liquid, remelting will first lead to a decrease in the diameter of the grain. Once the size class of the equiaxed grains due to remelting becomes smaller than the critical value of the grain size ($d_{e,critical}$), the equiaxed grains will be destructed. The destruction rate for the grains can be calculated using

$$n_{des} = v_R \frac{dn_{eq}}{dx} |_{x = d_{e,critical}}, \tag{9}$$

with

$$\frac{dn_{eq}}{dx} = \frac{n_{eq}}{\sqrt{2\pi} \cdot \sigma \cdot x} \cdot e^{-\frac{1}{2} \cdot \left(\frac{\ln(x) - \ln\left(\hat{d}_e\right)}{\sigma}\right)^2}, \tag{10}$$

where σ is the geometric standard deviation of the lognormal distribution, the dummy variable (x) corresponds to the equiaxed grain diameter of different size classes, and $\hat{d}_e$ is the geometrical mean of the grain size. However, only the volume-averaged grains diameter d_e, which is not equal to $\hat{d}_e$, could be obtained through the volume-averaged method. Thus, a further assumption was made in this study, the variation in d_e and $\hat{d}_e$ due to remelting follows the same trend, i.e., $d(\hat{d}_e)/dt \approx d(d_e)/dt$, which can be estimated by remelting rate of equiaxed grains (v_R).

2.3. One-way coupling of the electromagnetic field and flow field

A one-way coupling approach between the electromagnetic field and flow field was adopted. The electromagnetic field was calculated using ANSYS Maxwell, and the flow field was solved using ANSYS Fluent.

Firstly, the time-averaged Lorentz force was calculated using ANSYS Maxwell,

$$\vec{F} = \frac{1}{2}\left(\vec{J} \times \vec{B}^*\right). \tag{11}$$

The Lorentz force is composed of the forces in three directions (F_x, F_y, and F_z), but it acts mainly in the x direction. Thus, to consider the relative motion between the Lorentz force in the x direction (F_x) and the x-velocity component of the melt/equiaxed phase, F_x was modified using

$$F'_x = F_x \cdot \left(1 - \frac{u_x}{u_{B,x}}\right), \tag{12}$$

where F'_x is the modified Lorentz force in the x direction, u_x is the x-velocity of the melt/equiaxed phases, and $u_{B,x}$ is the moving velocity of the TMF. The Lorentz forces in other two directions (F_y, F_z) would keep as original. Then, the Lorentz forces (F'_x, F_y, F_z) were weighted by the corresponding phase volume fraction (f_ℓ, f_e) and finally used as the source terms ($F'_{x,\ell}$, $F'_{x,e}$, $F_{y,\ell}$, $F_{y,e}$, $F_{z,\ell}$, $F_{z,e}$) for the momentum conservation equations of each phase via User-Defined Functions (UDFs).

$$F'_{x,\ell} = F'_x \cdot f_\ell, \;\; F'_{x,e} = F'_x \cdot f_e, \tag{13}$$

$$F_{y,\ell} = F_y \cdot f_\ell, \;\; F_{y,e} = F_y \cdot f_e, \tag{14}$$

$$F_{z,\ell} = F_z \cdot f_\ell, \;\; F_{z,e} = F_z \cdot f_e, \tag{15}$$

3. Benchmark configuration

3.1. Experimental procedure

The experiments were conducted by another research group at the SIMAP Laboratory in Grenoble, France [20]. The Sn-10 wt.% Pb alloy was solidified in a quasi-two-dimensional rectangular ($100 \times 60 \times 10$ mm^3) mold. As shown in Fig. 2(a), two heat exchangers were arranged beside the two lateral walls of the sample to control the input/extraction of the heat. The heating and cooling history of the two exchangers designed for the experiment is

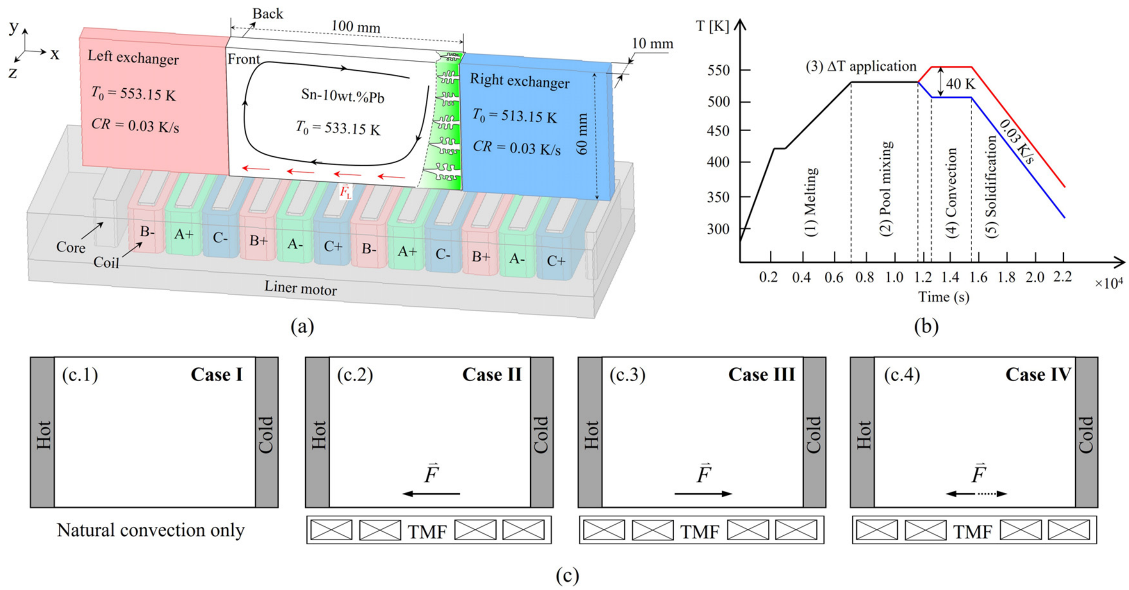

Fig. 2. (a) Schematic view of the experimental facility used for the benchmark [20]; (b) heating and cooling history of the two exchangers; (c) four different stirring modes. (c.1) Case I: natural convection only; (c.2) Case II: TMF aligned along the same direction as the natural convection; (c.3) Case III: TMF aligned along the opposite direction as the natural convection; (c.4) Case IV: TMF imposed in an alternative direction with a frequency of 0.0625 Hz (stirring in one direction for 8 s)

demonstrated in Fig. 2(b). A temperature difference of 40 K was assigned between the two exchangers during the cooling stage, and the cooling rates were equal to 0.03 K/s. An array of fifty thermocouples was placed onto the front surface of the sample to record the temperature evolution. A second array of sixteen thermocouples was arranged onto the back surface to confirm that the temperature variations in the thickness direction remain small, i.e., the temperature field of the sample follows a quasi-two-dimensional pattern. Nine thermocouples were arranged onto the left and right exchangers, respectively, to measure the heat flux extracted from the sample. As presented in Fig. 2(a), the linear motor used to generate the TMF was placed 5 mm beneath the sample. A three-phase alternative current (AC) with a constant frequency (f = 50 Hz) and current intensity (I = 8.2 A) was used to feed the power. For a more detailed introduction of the benchmark setup, refer to [20].

Once the coils were charged, a magnetic field was produced. If a conductive casting sample was loaded, an induced current was generated in the sample. The interaction between the magnetic field and induced current produced a Lorentz force, which drove the liquid to flow. The magnetic flux density (B) was measured along the x-axis (3 mm above the motor) without loading the sample. As schematically shown in Fig. 2(c), four different solidification experiments for Sn-10 wt.% Pb alloy were performed to investigate the effect of different types of forced convection on the as-cast structure and macrosegregation.

During the solidification process, evolutions of the temperature field were recorded and analyzed. Temperature maps for the selected area (x: 0.5 cm–9.5 cm; y: 1–5 cm) of the front surface (Fig. 2(a)) at three different solidification times (t = 540 s, t = 900 s, and t = 1440 s) were revealed [20]. t = 0 s corresponds to the first appearance of the liquidus of the alloy with an initial composition of c_0. After the castings completely solidified, the as-cast structures for the four cases were obtained through metallurgic analyses, which consisted of several passes of polishing with abrasive paper and chemical attack with a mixture of 75% Vol HCl (37 mol%/v) and 25% Vol HNO_3 (69.5%) [15]. A chemical method coupled using the Inductive Coupled Plasma (ICP) technique was used to obtain the quantitative results for the solute distribution, and the profiles for the macrosegregation were revealed by X-ray analysis along the thickness direction [20].

3.2. Numerical procedure

A full-scale inductor (Fig. 2(a)) was built to perform the electromagnetic calculation using the commercial software ANSYS Maxwell. Firstly, the magnetic field (B) along the x-axis without sample loading was calculated and compared with the measurements. Then, the conductive casting sample ($\sigma = 1.86 \times 10^6\ \Omega^{-1}\ m^{-1}$) was loaded 5 mm above the linear motor. The time-averaged $\vec{F}$ was calculated by solving Maxwell's equations, and the extracted $\vec{F}$ was interpolated into the mesh system of ANSYS Fluent. F_x was modified by multiplying $(1\text{-}u_x/u_{B,x})$ to consider the relative motion between the Lorentz force in the x direction and the x-velocity component of the corresponding phase (Eq. (12)). It was then weighted by the corresponding phase volume fraction (f_ℓ, f_e) and used as a source term in the momentum conservation equations for each phase (Eqs. (13) to (15)). Unlike the electromagnetic field calculation, only the casting domain was solved for the flow and solidification. Four simulations corresponding to Hachani's four experiments (Cases I-IV) [20] were conducted. The simulations started from the last stage (solidification) in Fig. 2(b), and the melt was assumed to have a homogeneous temperature (T = 533.15 K) and concentration (Sn – 10 wt.% Pb) distribution before solidification. A convective heat transfer boundary condition (h = 2000 $W/m^2{\cdot}K$) was used for the two lateral walls. At the beginning of the simulation, the left exchanger temperature was set as 553.15 K, and the right exchanger was set as 513.15 K. The cooling rate for the right exchanger was set to be 0.03 K/s, which is identical to the experimental value. The cooling rate for the left exchanger was experimentally reported to be 0.03 K/s, but here it was set to be 0.033 K/s. The reason for this modification will be discussed in detail in §5.4. Adiabatic boundary conditions were used for the remaining four walls. The liquid was assumed to be incompressible with a constant density and viscosity. The no-slip flow boundary condition was applied for the melt and equiaxed grains along all the sample walls. The thermodynamic/physical properties used in the current simulations are listed in Table 1.

A hexahedron mesh with a mesh size of 1 mm was used in the current study, and the total mesh number was 60,000. Regarding the flow calculation, for each timestep (Δt = 0.005 s),

Table 1
Thermo-dynamic/physical properties.

Property/parameters	Symbol	Units	Values	Ref.
Nominal Pb concentration of the alloy	c_0	wt.%Pb	10.0	[20]
Liquidus temperature (Sn-10 wt.%Pb)	T_{liq}	K	492.61	[20]
Melting temperature of pure Sn	T_f	K	505.15	[20]
Initial temperature	T_0	K	533.15	[20]
Partition coefficient	k	-	6.56×10^{-2}	[20]
Liquidus slope	m	K (wt.%Pb)$^{-1}$	-1.2826	[20]
Eutectic temperature	T_{eut}	K	456.57	[20]
Eutectic concentration	c_{eut}	wt.%Pb	38.1	[20]
Reference density	ρ_{ref}	kg m^{-3}	7000.0	[20]
Liquid density (buoyancy force)	ρ_ℓ	kg m^{-3}	$\rho_{ref}(1-\beta_T(T_\ell - T_{ref})-\beta_C(c_\ell - c_{ref}))$	
Solid density for both solid phases	ρ_e, ρ_c	kg m^{-3}	7310.0	
Thermal expansion coefficient	β_T	K^{-1}	6.0×10^{-5}	[17]
Solutal expansion coefficient	β_C	(wt.%Pb)$^{-1}$	-5.3×10^{-3}	[17]
Primary dendrite arm spacing	λ_1	m	2.25×10^{-4}	[35]
Secondary dendrite arm spacing	λ_2	m	6.5×10^{-5}	[17]
Diffusion coefficient in liquid	D_ℓ	m^2 s^{-1}	4.5×10^{-9}	[35]
Latent heat	L	J kg^{-1}	6.1×10^4	[17]
Specific heat	c_p^ℓ, c_p^e, c_p^c	J (kg K)$^{-1}$	260.0	[17]
Thermal conductivity	k_ℓ, k_e, k_c	W(m K)$^{-1}$	55.0	[17]
Viscosity	μ_ℓ	Pa s	1.0×10^{-3}	[20]
Gibbs-Thomson coefficient	Γ	m K	6.5×10^{-8}	[35]
Solid fraction in the dendritic envelope	f_{si}	-	0.5	[35]
Packing limit		-	0.637	[35]

*Super/subscripts ℓ, e, and c indicate different phases.

40 iterations were needed to decrease the normalized residuals for the continuity, momentum conservation equations to values below the convergence limit of 10^{-4} and those for the enthalpy conservation equations to below 10^{-7}. All simulations were performed in parallel using a high-performance computing cluster (2.6 GHz, 28 cores). One three-dimensional (3D) calculation required 7 days of computing time.

4. Simulation results

4.1. B field and distribution of the Lorentz force

Fig. 3(a) shows a comparison of the B field along the x-axis (3 mm above the motor) determined by calculation and measurement in the absence of the casting sample. Satisfactory agreement is obtained between the two datasets. The oscillation of the B field is caused by the arrangement of the magnets at the bottom of the device. The distribution of the time-averaged Lorentz force on the casting (solid-state with no movement) surface of Case II is shown in Fig. 3(b). The profile of the magnitude ($|F|$) of the Lorentz force along Line 1 (Fig. 3(b)) is plotted in Fig. 3(c). The maximal $|F|$ (728 N/m^3) appears at the bottom of the sample, and it exponentially declines along the sample height. The effective zone for the Lorentz force is limited to within a distance of 10 mm above the sample bottom.

4.2. Solidification sequence

To illustrate the TMF-induced flow and its effect on the formation of the as-cast structure and macrosegregation, the solidification sequence was analyzed for the middle vertical section based on Case II shown in Fig. 4. In this case, the Lorentz force acts in the same direction as natural convection. Schematic views of the liquid flow pattern and solidification process are shown in Fig. 4(a.x). Fig. 4(b.x) shows the calculated temperature field. The liquid velocity overlaid with f_c and the equiaxed velocity overlaid with f_e are presented in Fig. 4(c.x),(d.x), respectively. Fig. 4(e.x) shows the contour of $M_{\ell e}$ to demonstrate the simultaneous solidification and remelting phenomena. The induced macrosegregation profiles are displayed in Fig. 4(f.x).

The simulation results at 180 s are shown in Fig. 4(a.1)–(f.1). As the superheat dissipates from the right wall, the temperature gradually drops below the liquidus temperature on the right side (Fig. 4(b.1)). The red isoline of the constitutional undercooling ($\Delta T = T_f + m \cdot c_\ell - T$) that equals 0 K is plotted to separate the superheated and undercooling zones. The columnar dendrites initialize from the right wall and grow along the direction of the temperature gradient (Fig. 4(c.1)). A clockwise flow pattern is formed under a combination of the thermo-solutal buoyancy and Lorentz force of the TMF (Fig. 4(c.1)). The maximum liquid velocity ($\vec{u}_{\ell,max} = 0.1$m/s) is observed near the bottom-left corner.

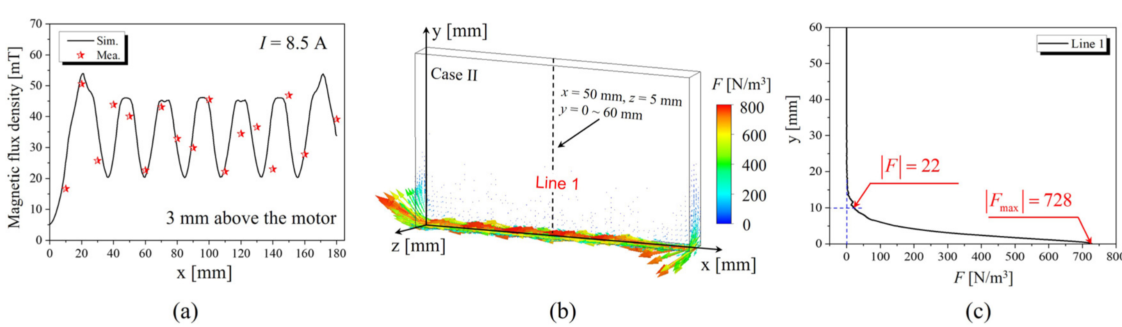

Fig. 3. (a) Comparison of the measured and calculated B in the absence of the casting sample along the x-axis (3 mm above the linear motor); (b) distribution of the time-averaged Lorentz force on the casting surface of Case II; (c) profile of the magnitude ($|F|$) of the Lorentz force along Line 1 shown in (b).

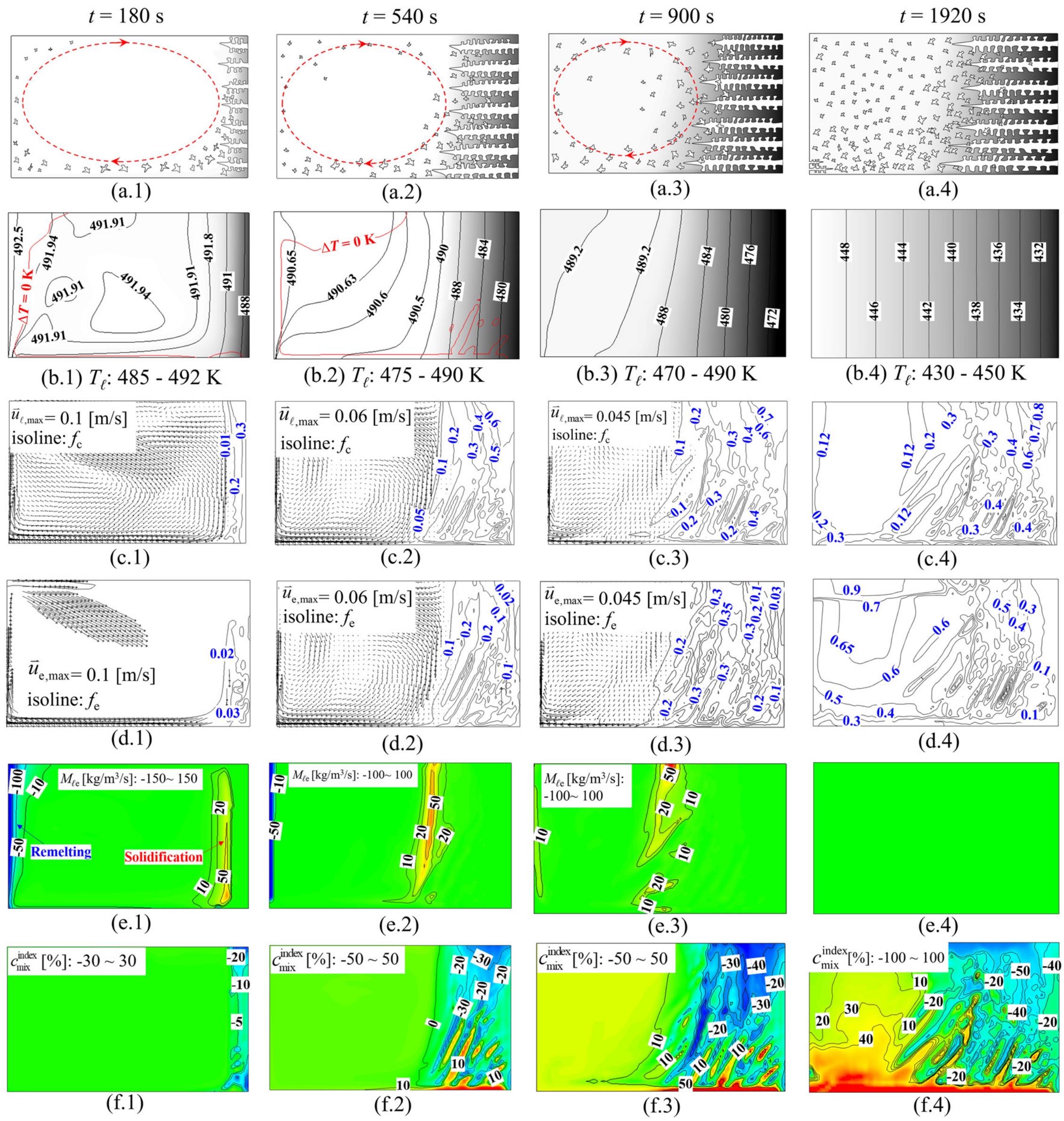

Fig. 4. Solidification sequence (on the middle vertical plane) of Case II: (a.x) Schematic views of the liquid flow pattern and dendrite growth; (b.x) contour and isolines (in black) of T (in K) overlaid with the red isoline of $\Delta T = 0$ K; (c.x) liquid velocity overlaid with the isolines of f_c; (d.x) velocity of equiaxed grains overlaid with the isolines of f_e; (e.x) contours of $M_{\ell e}$, red for solidification and blue for remelting; (f.x) contours of c_{mix}^{index}[%], red for positive segregation and blue for negative segregation.

In the columnar-liquid mushy zone, especially near the columnar tip region, the equiaxed grains are generated through fragmentation (Fig. 4(d.1)). At this moment, because the equiaxed grains are much heavier than the liquid melt, i.e., the density difference between the equiaxed grains and liquid melt ($\Delta\rho$) is positive ($\Delta\rho = \rho_e - \rho_\ell > 0$), the grains tend to sediment to the bottom of the sample. Due to the strong TMF-induced flow, some equiaxed grains are brought to the left superheated region (Fig. 4(d.1)), whereas the grains that are generated in or are brought to the deep mushy zone ($f_c > 0.2$) are captured by the columnar phase. From Fig. 4(b.1) and 4(e.1), the equiaxed grains grow ($M_{\ell e} > 0$) in the undercooled melt near the solidification front and remelt ($M_{\ell e} < 0$) in the left superheated liquid. A slightly negative segregation is observed along the right wall (Fig. 4(f.1)).

At 540 s, the sample is further cooled down (Fig 4(b.2)). The columnar dendrites grow to 1/3 of the sample width, and f_e is increased to 20% (Fig. 4(c.2),(d.2)). Although the superheated region (e.g., the lower-right and upper-left corners) is extended due to the enrichment of the solute in the bulk liquid, the maximum superheat is decreased by 1.29 K compared to the results obtained at 180 s. Similar to the results shown in Fig. 4(e.1), remelting of equiaxed grains occurs mainly near the left wall, but the remelting rate is significantly reduced in Fig. 4(e.2). At this moment, some channel segregations initialize from the right-bottom region of the mushy zone (Fig. 4(f.2)).

The superheat is totally dissipated from the sample (Fig. 4(b.3)) at 900 s. The columnar dendrites and equiaxed grains grow competitively in the remaining undercooled melt. The enrichment of the solute element (Pb) in the melt (Fig. 4(f.3)) makes the liquid melt denser, which decreases the $\Delta\rho$ and even reverses it ($\Delta\rho < 0$), i.e., the liquid melt is heavier than the equiaxed grains. It becomes easier for equiaxed grains to float upwards along the left wall of the sample (Fig. 4(d.3)). Some of the equiaxed grains are brought back to the columnar tip front. The growth of such

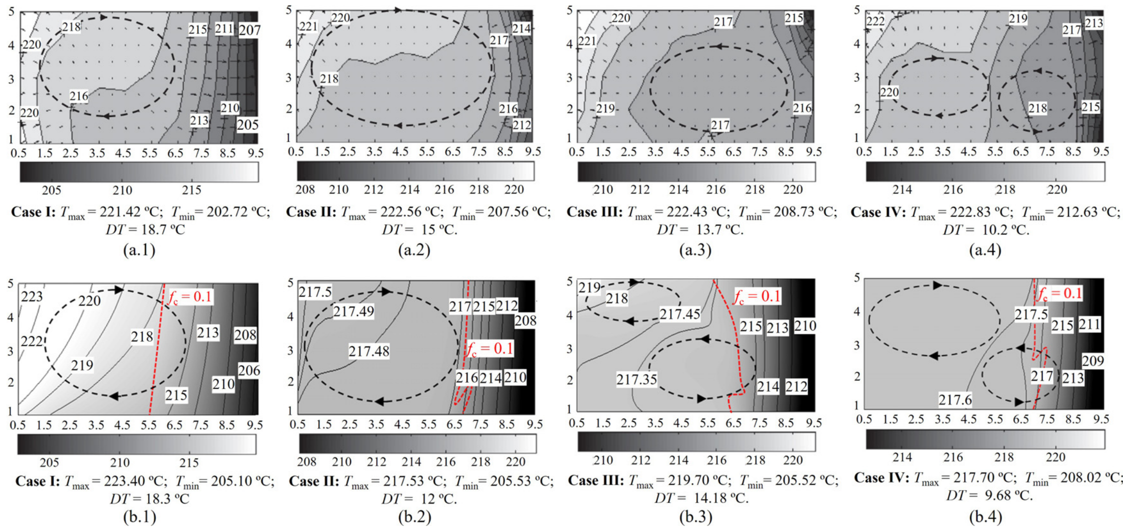

Fig. 5. Comparison of the temperature field (in°C) for the four cases (I - IV) determined by measurements and the simulation for the front surface of the sample at 540 s, (a.x) the measurement results, (b.x) the simulation results. The black dashed lines show the direction of the liquid convection, and the red dashed lines show the position of the solidification front (isoline of $f_c = 0.1$). (a.x) is reprinted from publication [20], with permission from Elsevier.

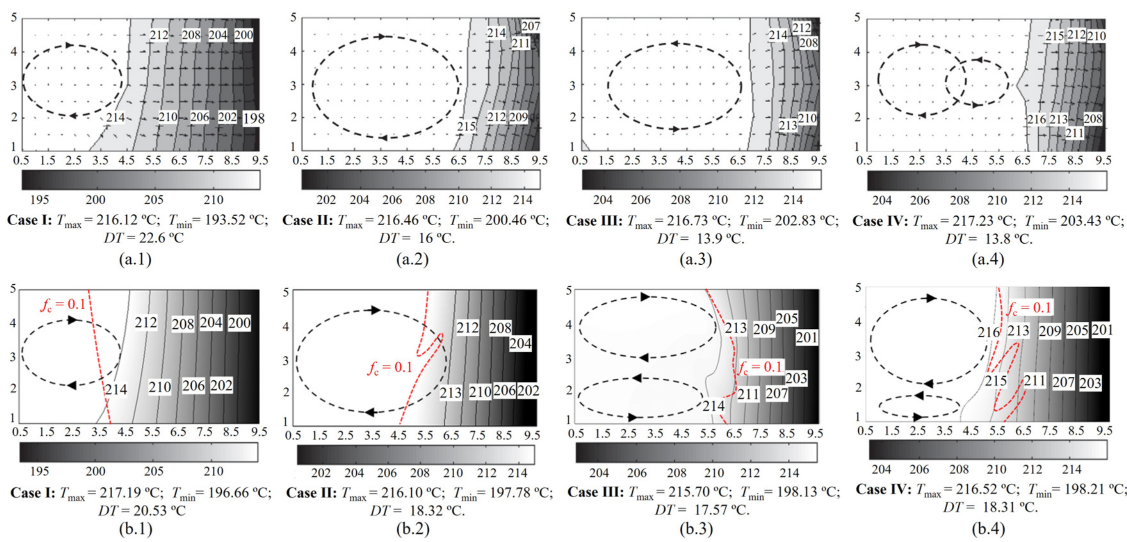

Fig. 6. Comparison of the temperature field (in°C) for the four cases (I - IV) determined by measurements and simulation for the front surface of the sample at 900 s, (a.x) the measurement results, (b.x) the simulation results. The black dashed lines show the direction of the liquid convection, and the red dashed lines show the position of the solidification front (isoline of $f_c = 0.1$). (a.x) is reprinted from publication [20], with permission from Elsevier.

equiaxed grains inhibits the advancement of the columnar dendrites accordingly (Fig. 4(c.3)), leading to the columnar-to-equiaxed transition (CET).

The sample is fully solidified at 1920 s. As presented in Fig. 4(c.4), the columnar dendrites take the right side, and the remaining part is mostly occupied by the equiaxed grains. In the upper left corner of the sample (Fig. 4(d.4)), the sample is solidified as a fully equiaxed grain structure. Serious positive segregation is found in the lower-left corner, which indicates the presence of a high-volume fraction of eutectics. Several channel segregations can be observed in the lower-right corner (Fig. 4(f.4)).

4.3. Calculated temperature fields and comparison with experiments

Comparison of the temperature field determined from the measurement and simulation results for all four cases (I - IV) for the selected area of the front surface (x: 0.5 cm–9.5 cm; y: 1 cm–5 cm) at three different solidification times are shown in Fig. 5–7. The DT is defined as the difference between the maximum temperature and the minimum temperature of the measured region. The solidification front is indicated by the isoline of $f_c = 0.1$ in the simulation results. Satisfactory agreements between the measurements and simulation results are obtained.

As shown in Fig. 5(a.1)–5(b.1), in Case I, the isotherms are distorted following the direction (clockwise) of the fluid flow. The maximum temperature appears at the top-left corner, and the measured and calculated DT values are equal to 18.7°C and 18.3°C (Fig. 5(a.1),(b.1)), respectively. Compared to Case I, the enhanced convection due to the TMF in Case II leads to a more uniform temperature field, i.e., the measured DT is decreased from 18.7 to 15°C (Fig. 5(a.2)), and the calculated DT is decreased from 18.3 to 12°C (Fig. 5(b.2)). For Case III, the reversed forced convection (the anticlockwise vortex at the lower part of the sample in Fig. 5(b.3)) bends the isotherms to the right side in the lower part of the sample. The DT for this case is decreased to 14°C. According to the simulation results, the maximum temperature in the top-left corner of Case III is caused by another small clockwise vortex, which is de-

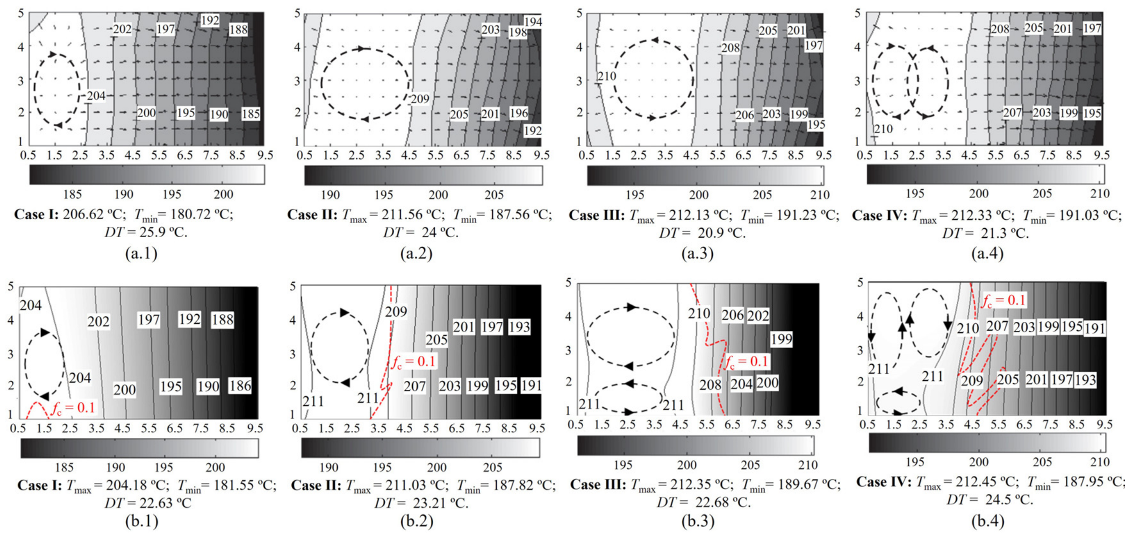

Fig. 7. Comparison of the temperature field (in°C) for the four cases (I - IV) determined by measurements and simulation for the front surface of the sample: (a.x) the measured results at 1440 s, (b.1) the simulation results at 1440 s, (b.2) the simulation results at 1280 s, (b.3) the simulation results at 1200 s, and (b.4) the simulation results at 1300 s. The black dashed lines show the direction of the liquid convection, and the red dashed lines show the position of the solidification front (isoline of $f_c = 0.1$). (a.x) is reprinted from publication [20], with permission from Elsevier.

veloped in the top-left part (Fig. 5(b.3)). For Case IV, two vortices with different flow directions are predicted. Their flow directions vary with time due to the periodic change in the Lorentz force. Comparing the DT for the four cases, the periodically reversed stirring mode shows the highest efficiency in homogenizing the temperature field.

The measured and calculated temperature field at 900 s is shown in Fig. 6. The measured temperature field (isotherms and DT) for the four cases can also be well "reproduced" by the simulations. Because of the reduced liquid flow velocity in the mushy zone, the isotherms are almost vertical on the right side. Regarding DT, a similar trend to that for the previous time (540 s) is found, i.e., the TMF tends to homogenize the temperature by decreasing DT.

At 1440 s (Fig. 7), it is interesting to note the existence of isotherms corresponding to the temperature level ranging from 204 to 210°C on the left side, which indicates that the initial heat flux flowing into the sample from the left wall is reversed to flow out of the sample. This condition is favorable for the onset of the second solidification front from the left wall.

Notably, the indicated flow patterns at three solidification times in Case III are different for the experiment and the simulation. One more vortex is found in the liquid pool by the simulation.

4.4. As-cast structure

The metallographic analysis of the as-cast structures in the laboratory experiment is shown in Fig. 8(a.x). The calculated distributions of f_c and f_e are depicted in Fig. 8(b.x),(c.x). Satisfactory simulation-experiment agreements are achieved for Cases I, II, and IV but not for Case III. The mismatch for Case III will be discussed in detail in §5.3. For Case I, Fig. 8(a.1),(b.1), the upwind tilting of the columnar dendrites dominates the as-cast structure, and the equiaxed grains are mainly distributed in the segregation channels and in a band on the left part of the sample (Fig. 8(c.1)). For Case II, the equiaxed zone is greatly extended (Fig. 8(a.2)) compared to Case I. The left half of the sample is solidified as equiaxed grains (Fig. 8(c.2)), and the right half is solidified as columnar dendrites (Fig. 8(b.2)). For Case IV, the equiaxed region is further extended (Fig. 8(a.4) and (c.4)), and columnar dendrites are facilitated in the two right-hand corners (Fig. 8(b.4)).

4.5. Macrosegregation

The experimentally measured macrosegregation profiles obtained by X-radiography and digital processing methods are shown in Fig. 9(a.x), (b.x), respectively. The calculated segregation profiles obtained by averaging the Pb concentrations for ten cross-section planes along the thickness direction are presented in Fig. 9(c.x). The simulation results agree well with the experimental measurements except for Case III. The possible reason for this mismatch in Case III will be discussed in detail in §5.3. For Cases I, II, and IV, several channel segregations [24–25,49–50] are formed in the right part of the sample. Negative segregation is mainly observed in the upper right region, and positive segregation locates in the left-bottom region. Compared to the result of Case I (Fig. 9(a.1),(c.1)), the location of the strongest positive segregation is pushed to the left-bottom corner in Case II (Fig. 9(a.2),(c.2)), while the periodically reversed convection (Case IV) is observed to shift this positive segregation to the central-bottom area (Fig. 9(a.4),(c.4)). By integrating the macrosegregation index in the calculation domain, the global macrosegregation index ($\mathrm{GMI} = \iiint_{\mathrm{vol}} |c_{\mathrm{mix}}^{\mathrm{index}}| dv$) is determined to be 38.17% for Case I. By applying the TMF, the GMI is increased to 39.45% for Case II and 39.77% for Case IV. It is found that macrosegregation is generally intensified by the TMF.

3D views of the simulated channel segregations for the four cases are revealed by the isosurface of $c_{\mathrm{mix}} = 11$wt.%Pb, as shown in Fig. 10. The results are colored by c_{mix} from 2 wt.% Pb to 18 wt.% Pb. Channel segregations are clearly observed for the four cases. The TMF leads to an increase in the number of channel segregations (Fig. 10(b), (d)).

As mentioned above, Case III cannot be well reproduced in the current study. Good agreement has been achieved for Case I, as reported previously [39]. Here, a quantitative comparison of the Pb concentration determined from simulation results and measurements focuses on Case II and Case IV, as shown in Fig. 11 and 12. Fifty cores (yellow dots in Fig. 11(a) and 12(a)) distributed along five horizontal lines were extracted by drilling holes (ϕ 0.5 cm × 1 cm) from the as-solidified sample along the thickness direction. A chemical method coupled with the Inductive Coupled Plasma (ICP) technique was used to determine the mean value for the Pb concentration at each point. The simulated Pb concentrations (blue

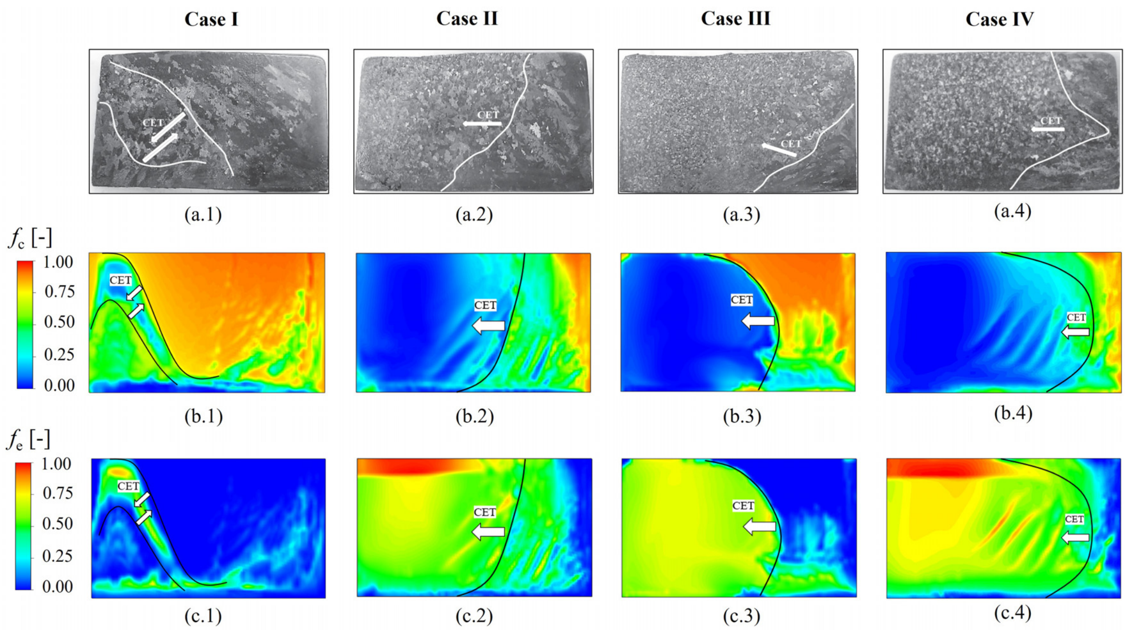

Fig. 8. Comparison of the as-cast structure for the four cases (I - IV) based on metallographic analysis in laboratory experiments (a.x) and the simulated volume fraction of columnar dendrites (b.x) and equiaxed grains (c.x). (a.x) is reprinted from publication [20], with permission from Elsevier.

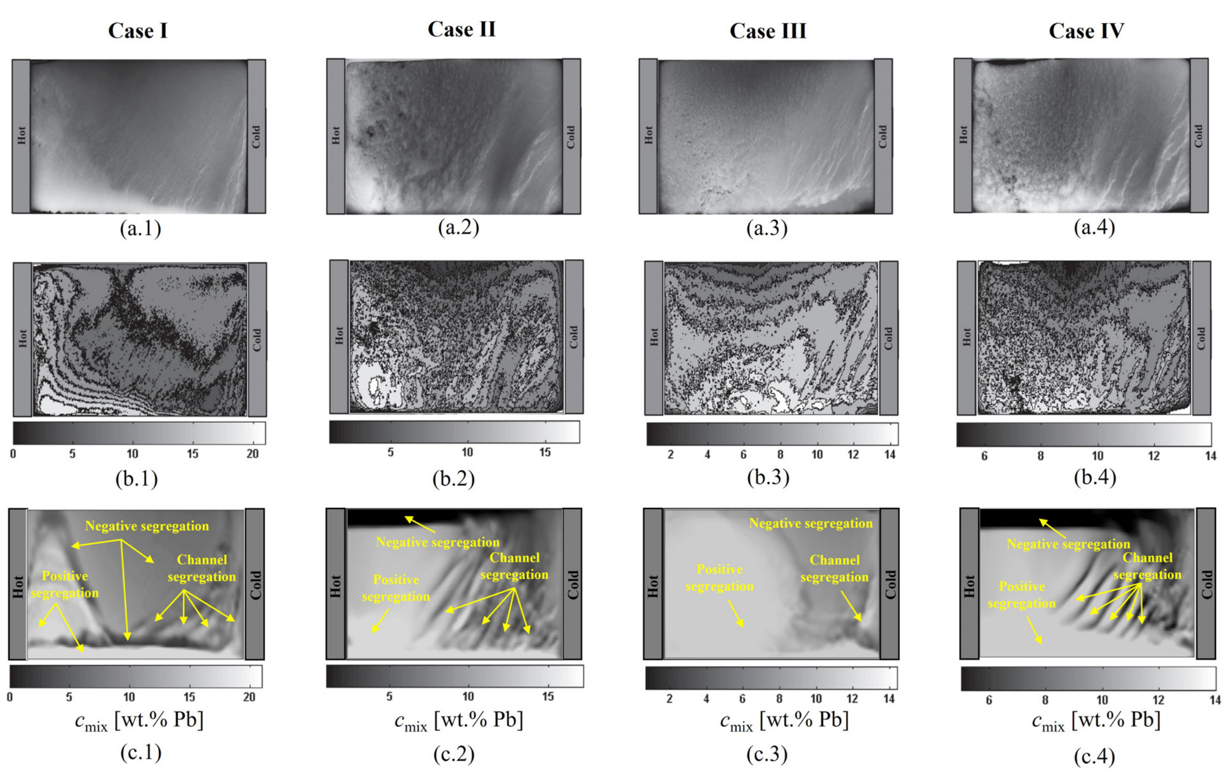

Fig. 9. Macrosegregation maps obtained for the sample under the effect of different electromagnetic stirring modes: (a.x) X-radiography of the as-solidified ingot; (b.x) Pb concentration map digitally processed from (a.x); (c.x) simulated mean Pb concentration through the thickness direction. (a.x) and (b.x) are reprinted from publication [20], with permission from Elsevier.

box), averaged in the volumes (0.4 cm × 0.4 cm × 1 cm) corresponding to the same positions of the experiment, are compared with those of the experiment in Fig. 11 and 12. The simulated results coincide with the measurement results very well. A similar tendency for the macrosegregation distribution determined by the simulations and measurements is observed. To capture more information about the segregation, the mean concentrations along the five horizontal lines (Fig. 11(a), 12(a)) are also plotted. The simulation curves also show a good agreement with the measurement results. Nevertheless, the fluctuation of the red lines, which indicates the channel segregation, cannot be detected by using this analysis method. The reason for this is due to the core size (ϕ 0.5 cm) of the chemical analysis, which is too large for capturing the channel segregation phenomena.

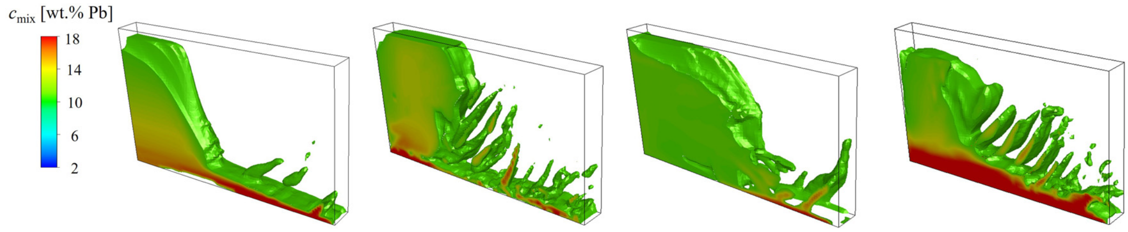

Fig. 10. 3D views of the isosurfaces of $c_{mix} = 11$wt.%Pb for the four cases (I - IV). The results are colored by c_{mix}.

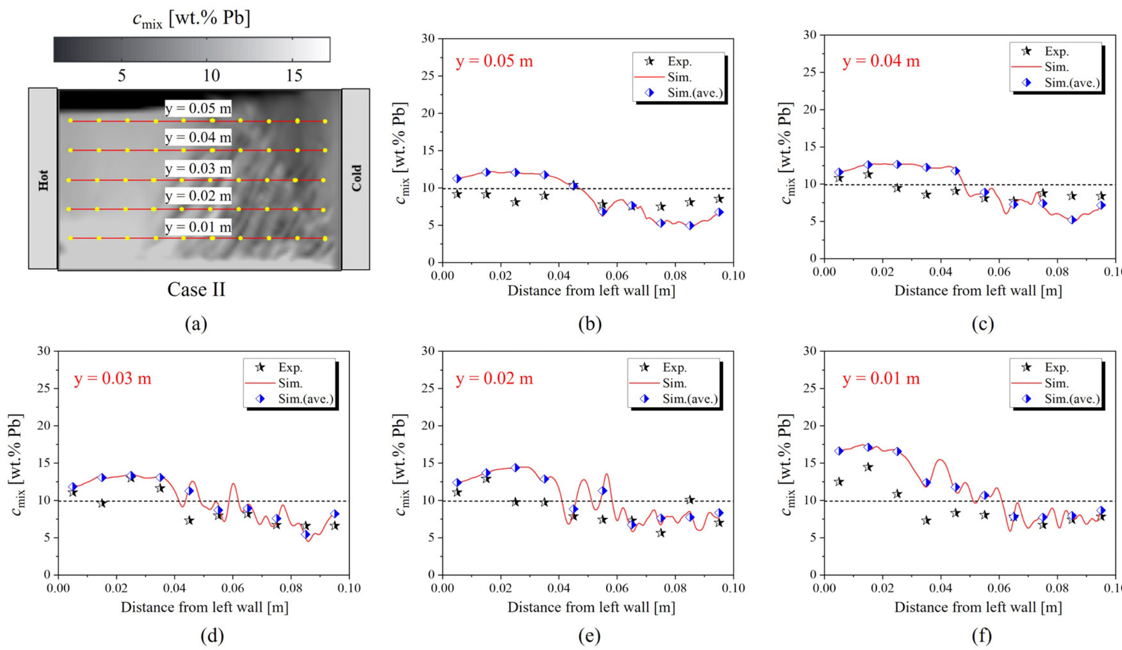

Fig. 11. Quantitative comparison of the Pb concentration (c_{mix}) for Case II determined from the measurement data obtained using the ICP (Inductive Coupled Plasma) technique and simulation results. (a) Contour of the simulated Pb concentration; (b)–(f) correspond to the results obtained at five different horizontal lines, y = 0.05, 0.04, 0.03, 0.02, and 0.01 m. The experimental points show the averaged Pb concentrations in the drilling holes (ϕ 0.5 cm × 1 cm). The points of simulation show the averaged Pb concentrations in the volumes (0.4 cm × 0.4 cm × 1 cm) corresponding to the experimental positions.

5. Discussion

5.1. Effect of TMF-induced convection on the evolution of the columnar tip front

Fig. 13 shows the profiles of the columnar tip front ($f_c = 0.01$) at the early stage of solidification ($t = 120$ s) for the four different cases. The isotherms overlaid with the liquid velocity in vector are plotted on the central vertical section.

For Case I, natural convection acts in the sample. The isotherms are distorted, and the lowest temperature appears at the bottom-right corner. The columnar dendrites solidify and extend to the left side (Fig. 13(a)). The profile of the columnar tip front is consistent with that of the isotherm. For Case II, natural convection is strengthened by the TMF. The isotherms are more distorted. The high-temperature melt coming from the upper-left corner impinges the middle part of the right cold wall. It, consequently, influences the isotherms near the columnar tip front, i.e., the temperature in the middle part of the right-cold wall is slightly higher than that at the two right-hand corners. Thus, the growth speed of the columnar tip front at the two right-hand corners is faster than that at the middle part of the right wall (Fig. 13(b)). Two vortices with opposite directions are formed in Case III (Fig. 13(c)): the first vortex locates on the left side in the clockwise direction, while the other one locates on the right side in the anticlockwise direction. This kind of flow pattern in Case III is not indicated by the experiment (Figs. 5(a.3), 6(a.3), 7(a.3)). The right-anticlockwise convection transports the cooler melt to the upper-right corner along the right wall. The lowest temperature appears at the upper-right corner, where the columnar tip front is facilitated to grow (Fig. 13(c)). When the periodically reversed stirring is applied (Case IV), the flow direction near the columnar tip front is also reversed periodically. When an anticlockwise flow is induced, the aggregation of the cooler melt at the upper-right corner promotes the growth of the columnar dendrites in this area. When a clockwise flow is induced, the growth of columnar dendrites at the bottom-right corner is accelerated. Thus, the columnar tip front preferentially grows from the two corners of the right wall (Fig. 13(d)).

Through the above analysis, it should be noted that the forced convection plays an important role in changing the temperature field and further influencing the evolution of the columnar tip front. The final as-cast structure and macrosegregation are closely associated with the flow patterns induced by different types of TMFs.

5.2. Importance of remelting/destruction of equiaxed grains

An additional simulation (Case II-A) was conducted to demonstrate the importance of the remelting/destruction of equiaxed

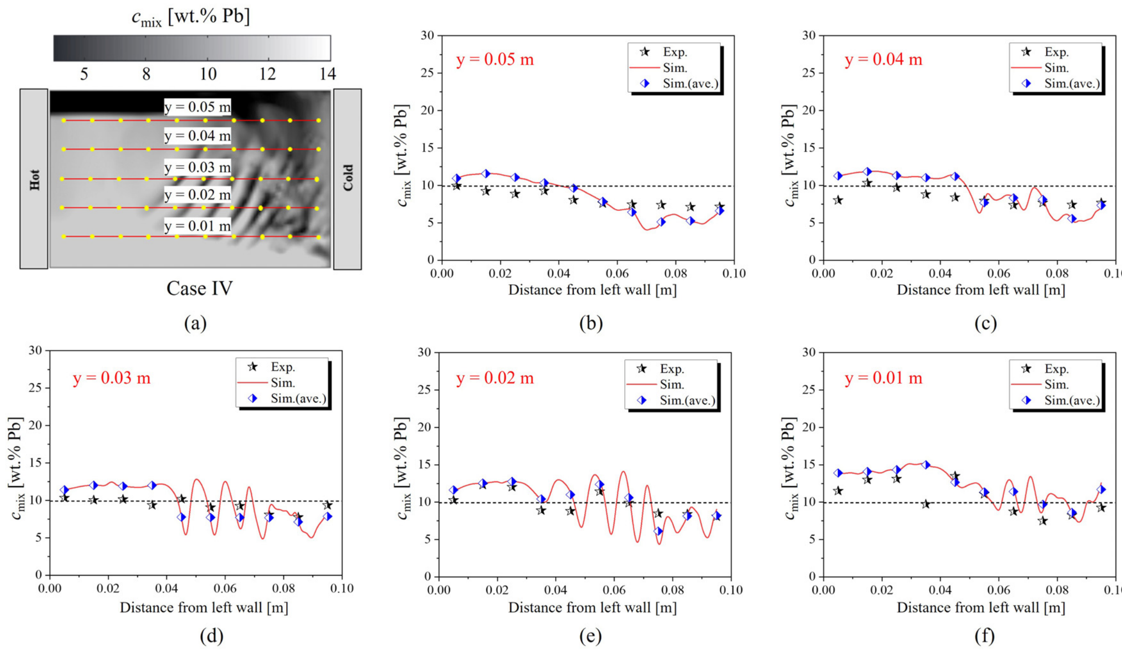

Fig. 12. Quantitative comparison of the Pb concentration (c_{mix}) for Case IV determined from the measurement data obtained using the ICP (Inductive Coupled Plasma) technique and simulation results. (a) Contour of the simulated Pb-concentration; (b)–(f) correspond to the results at five different horizontal lines, y = 0.05 m, 0.04 m, 0.03 m, 0.02 m, and 0.01 m. The experimental points show the averaged Pb concentrations in the drilling holes (ϕ 0.5 cm × 1 cm). The points of simulation show the averaged Pb concentrations in the volumes (0.4 cm × 0.4 cm × 1 cm) corresponding to the experimental positions.

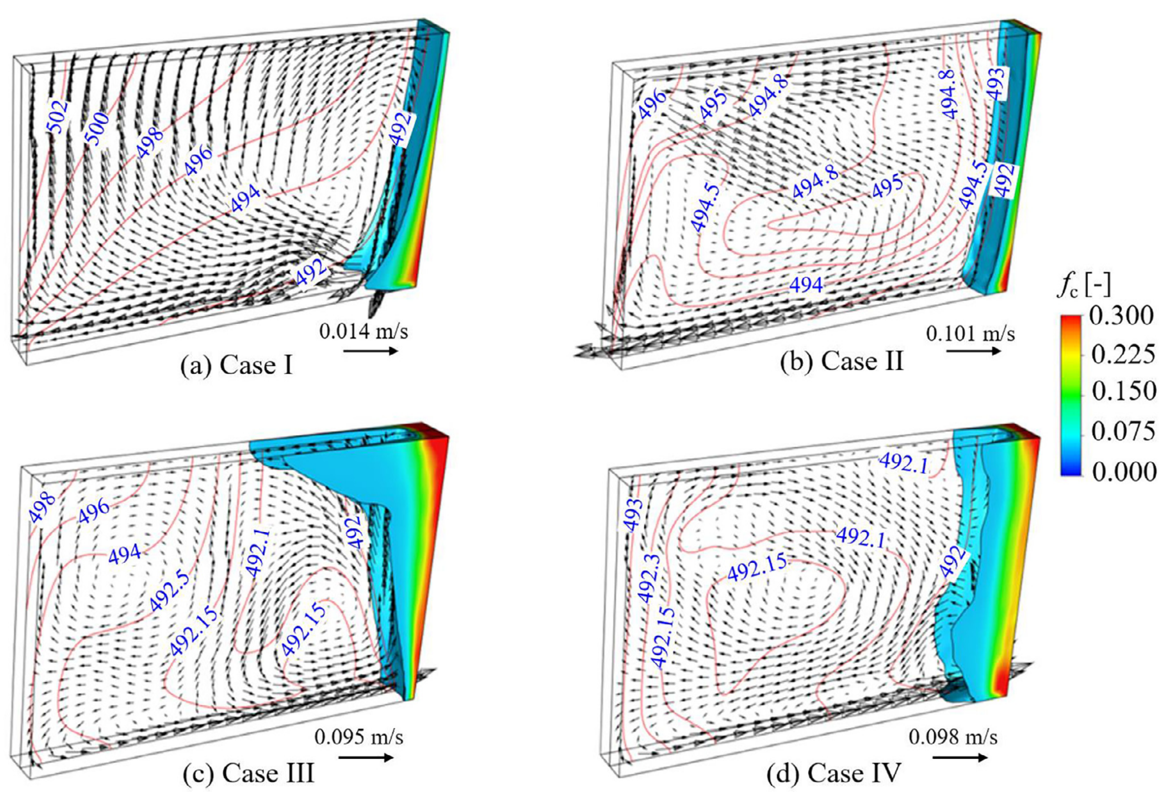

Fig. 13. Influence of TMF-induced convection on the columnar tip front, which is defined by the isosurface of f_c = 0.01 at the early stage of solidification (t = 120 s) for the four cases: (a) Case I; (b) Case II; (c) Case III; and (d) Case IV. The isotherms overlaid with the liquid velocity in vector are plotted on the central vertical plane of the sample.

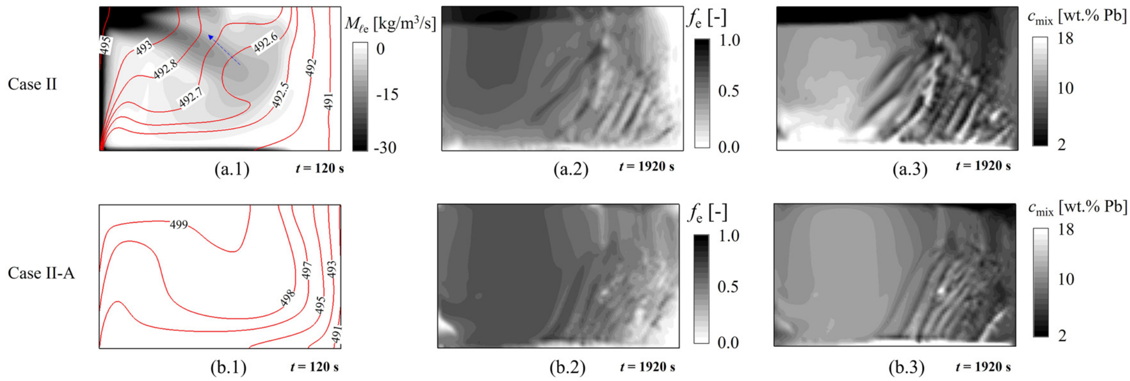

Fig. 14. Comparison of the simulation results obtained for the two cases (Case II and Case II-A) with (a.x) and without remelting of equiaxed grains (b.x); (a.1)-(b.1) contours of $M_{\ell e}$ (negative value due to remelting only) overlaid with isotherms at 120 s; (a.2)-(b.2) as-solidified structure of equiaxed grains (f_e) at 1920 s; (a.3)-(b.3) contours of the c_{mix} at 1920 s.

grains and its further impact on the temperature field, formation of the as-cast structure and macrosegregation. All the settings for Case II-A were the same as those for Case II except for ignoring the remelting/destruction of equiaxed grains. The simulation results obtained for Case II and a comparison with Case II-A are shown in Fig. 14. The net mass transfer rate from liquid to equiaxed ($M_{\ell e}$) due to remelting overlaid with the isotherms obtained at 120 s is shown in Fig. 14(a.1),(b.1). Only the range with a negative value, indicating the remelting process, is displayed. The equiaxed grains start to remelt if they are exposed in the superheated melt. By integrating $M_{\ell e}$ over the whole sample region, the remelting rate is determined to reach up to 4.8×10^{-4} kg/s. Correspondingly, the heat dissipation rate due to the consumption of the latent heat from the liquid melt by remelting is equal to 29.3 J/s. As shown in Fig. 14(a.1), the isotherms (e.g., 492.6 K and 492.7 K) are distorted in the area where remelting occurs. The average temperature of the liquid is overestimated by 5.13 K in Case II-A, ignoring remelting, compared to Case II, considering remelting of the equiaxed grains. The simulated distributions of f_e and c_{mix} in the as-solidified sample for the two cases are shown in Figs. 14(a.2),(b.2) and (a.3),(b.3), respectively. In comparison to Case II, (1) ignoring the remelting of equiaxed grains (Case II-A) leads to an overestimation of f_e by 15.3% (30.4 g) and an underestimation of f_c by 34.1% (30.6 g); (2) although some segregation channels are also predicted to be present, as shown in Fig. 14(b.3), the experimentally observed segregation pattern (i.e., the serious positive segregation at the left-bottom corner and the negative segregation at the left-top region, Fig. 9(b.2)), cannot be reproduced by Case II-A; (3) the GMI is underestimated by 48% for Case II-A. The accompanying remelting of equiaxed grains during the solidification process represents a significant species/energy transport mechanism. Ignoring the remelting phenomenon would lead to an overestimation of the temperature in the liquid melt. This leads to a further overestimation of the mass of the equiaxed grains and underestimation of macrosegregation.

5.3. Simulation-experiment mismatch in Case III

Based on the current numerical model, the experimental results, e.g., the temperature field, as-cast structure and macrosegregation, cannot be "reproduced" for Case III. One reason for this mismatch could be the avalanche phenomenon [51], which probably occurs when the columnar dendrites solidify from the upper-right corner of the ingot in the early stage of solidification. The current model cannot be used to consider this phenomenon.

The evolution of the columnar structure (Case III), which is represented by the isosurface of $f_c = 0.05$, is shown in Fig. 15. The temperature field overlaid with the liquid velocity in vector is displayed on the central vertical plane. At 50 s, the TMF-induced forced convection, which is in the anti-clockwise direction, transports the high temperature melt along the bottom toward the right cold wall. The melt impinges the bottom-right corner, and then flows to the upper part of the ingot along the right cold wall. The lowest temperature (T_{low} = 490.49 K), and the associated solidification of the columnar structure should start at the upper-right corner, as shown in Fig. 15(a). At 100 s, the columnar tip front continually grows and extends downwards along the cold wall. The flow pattern is slightly different from that found previously, i.e., the vortex in the upper-left corner is enlarged, while the main vortex is compressed to the right side (Fig. 15(b)). A zoomed view of the distribution of $\vec{u}_\ell \cdot \nabla c_\ell$ near the upper-right corner (Zone A marked in Fig. 15(b)) on the central vertical plane is shown in Fig. 15(c). The interdendritic flow ($\vec{u}_\ell$) in the direction opposite to the liquid concentration gradient (∇c_ℓ) leads to local remelting. The 'blue' region with a negative value of $\vec{u}_\ell \cdot \nabla c_\ell$, where the angle between $\vec{u}_\ell$ and ∇c_ℓ is larger than 90°, is observed near the right wall. If the remelting of columnar dendrite roots causes massive dendrites to fall off from the right wall, as schematically shown in Fig. 15(d), the avalanche phenomenon is likely to occur. However, this phenomenon is still far more complex for the recent model. According to the current model, the growth of the columnar dendrites in the upper-right part is further promoted during the later solidification stage. Finally, the as-solidified columnar dendrites capture the upper-right part of the sample in Case III (Fig. 8(b.3)), leading to a mismatch to the measurement result (Fig. 8(a.3)).

Another possible reason why the simulation result for Case III cannot reproduce the as-cast structure is that the heterogeneous nucleation is ignored. The significant role of fragmentation in the generation of equiaxed grains in this benchmark experiment has been addressed by Hachani et al. [20]. Thus, only the fragmentation of columnar dendrites is considered as the source of the equiaxed grains in the current study. However, heterogeneous nucleation, which can serve as another source of equiaxed grains, is likely to occur when the inoculants are exposed to the undercooling environment. Specifically, when the lowest temperature appears at the upper-right corner in the early solidification stage of Case III, the first solid phase can consist of columnar dendrites or equiaxed grains, which are formed through heterogeneous nucleation. If the equiaxed grains can occupy the upper-right corner during the later solidification process, the simulated final as-cast structure will show good agreement with the measurement result.

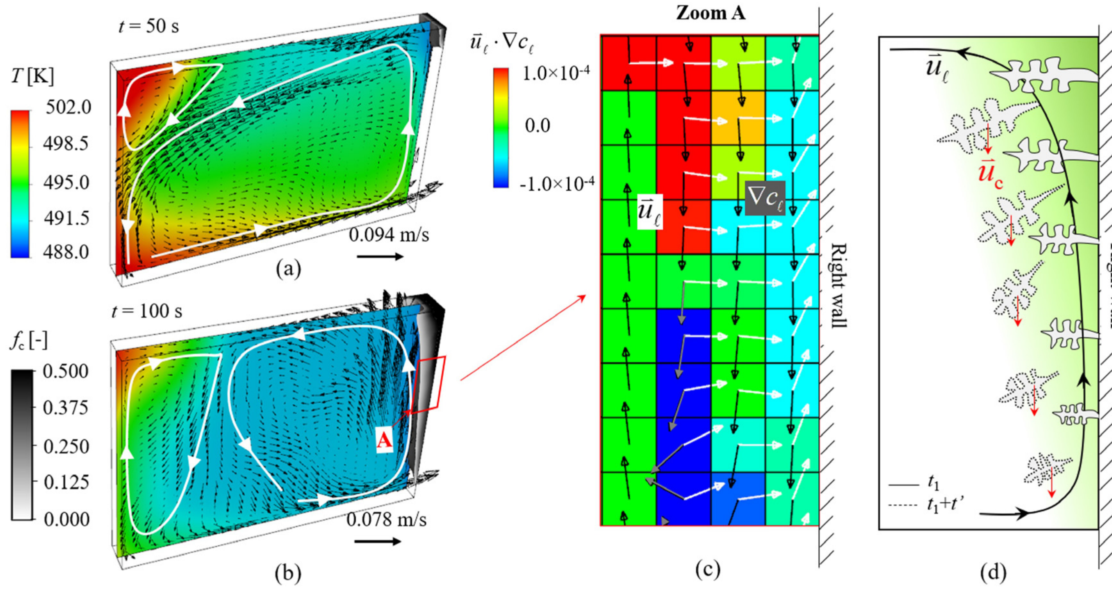

Fig. 15. Solidification sequence of the columnar dendrites (iso-surface of $f_c = 0.05$) for Case III: (a) $t = 50$ s; (b) $t = 100$ s; (c) zoom view of the $\vec{u}_\ell \cdot \nabla c_\ell$ distribution in Zone A shown in (b). Temperature field overlaid with liquid velocity vector is shown on the central vertical plane; (d) schematic view of the avalanche phenomenon.

5.4. Boundary conditions for the two lateral walls

The temperature history for the two exchangers was monitored during the solidification process [20]. However, due to the thermal contact resistance between the exchangers and sample walls, which is not always constant, the exact temperatures of the two lateral walls (T_{wall}) are unknown and need to be determined. The extrapolation method based on the heat reservation law can be used to calculate T_{wall} [31–32]. However, because the exact experimental temperature for the two exchangers is unknown, the use of this method is greatly limited for researchers.

The convective heat transfer boundary condition ($q = 2000 (T_{wall} - T_{exch})$) was used in the current study, where q is the heat flux between the sample and exchanger and T_{exch} is the defined exchanger temperature in Fig. 2(b). Based on the cooling rates (0.03 K/s) for the two exchangers provided by Hachani et al. [20], the isotherms corresponding to the temperature level ranging from 204 to 210°C on the left side of the four cases (I-IV) cannot be “reproduced”. Numerical parameter studies were performed by varying the cooling rate for the left exchanger. The best fit to the temperature fields for all four cases is obtained for a cooling rate value of 0.033 K/s (9% higher than 0.03 K/s). Consequently, this cooling rate was used in this study.

6. Conclusion

An extended three-phase mixed columnar-equiaxed solidification model was used to simulate the benchmark experiments for Sn-10wt.% Pb alloy [20]. Four cases under different flow conditions (natural convection and/or forced convection with different modes) were investigated. Except for Case III, satisfactory simulation-experiment agreements in terms of the temperature field, as-cast structure and macrosegregation were obtained for the remaining three cases. Based on the simulation results, the following conclusions are drawn.

(1) To ‘reproduce’ the benchmark experiments [20], the model must at least have the following features: i) three phases (liquid melt, equiaxed grains, and columnar dendrites); ii) dendrite fragmentation, which gives birth to the equiaxed grains; iii) movement of equiaxed grains; iv) growth and remelting/destruction of equiaxed grains exposed to undercooled and superheated liquid; and v) coupling between the TMF and multiphase flow.
(2) The simultaneous solidification and remelting of equiaxed crystals represent an important species/energy transport mechanism in this laboratory benchmark. Ignoring the remelting of equiaxed grains in the superheated region in a numerical model will lead to an error in the estimation of the as-cast structure and macrosegregation.
(3) TMF plays an important role in homogenizing the temperature field and promoting equiaxed grain formation through the fragmentation mechanism, and, consequently, facilitates CET.
(4) TMF is found to generally intensify macrosegregation and increase the number of channel segregations.

The simulation and experimental measurement results obtained for Case III show a mismatch most likely because the avalanche phenomenon and/or heterogeneous nucleation was not taken into account. Further modeling effort is still needed to ‘reproduce’ Case III.

Declaration of Competing Interest

The authors declare that they have no known competing financial interests or personal relationships that could have appeared to influence the work reported in this paper.

CRediT authorship contribution statement

Zhao Zhang: Conceptualization, Methodology, Software, Investigation, Writing – original draft, Validation, Visualization. **Menghuai Wu:** Conceptualization, Methodology, Software, Writing – review & editing, Project administration, Funding acquisition. **Haijie Zhang:** Methodology, Software. **Andreas Ludwig:** Resources, Supervision. **Abdellah Kharicha:** Software, Formal analysis.

Data availability

Data will be made available on request.

Acknowledgments

The authors acknowledge the financial support from the Austrian Research Promotion Agency (FFG) through the project Bridge I (No. 868070) as well as the technical support of the industrial partner Primetals Technologies Austria GmbH.

References

[1] K. Ayata, T. Mori, T. Fujimoto, T. Ohnishi, I. Wakasugi, Improvement of macrosegregation in continuously cast bloom and billet by electromagnetic stirring, Trans. Iron Steel Inst. Jpn. 24 (1984) 931–939, doi:10.2355/isijinternational1966.24.931.
[2] N.A. Shan, J.J. Moore, A review of the effects of electromagnetic stirring (EMS) in continuously cast steel, Part 1 Ironmak. Steelmak. 9 (1982) 31–36.
[3] S. Wang, G. Alvarez De Toledo, K. Välimaa, S. Louhenkilpi, Magnetohydrodynamic phenomena, fluid control and computational modeling in the continuous casting of billet and bloom, ISIJ Int. 54 (2014) 2273–2282, doi:10.2355/isijinternational.54.2273.
[4] N. Genma, T. Soejima, T. Saito, M. Kimura, Y. Kaihara, H. Fukumoto, K. Ayata, The linear-motor type in-mold electromagnetic stirring technique for the slab continuous caster, ISIJ Int. 29 (1989) 1056–1062, doi:10.2355/isijinternational.29.1056.
[5] K. Fujisaki, In-mold electromagnetic stirring in continuous casting, IEEE Trans. Ind. Appl. 37 (2001) 1098–1104, doi:10.1109/28.936402.
[6] K. Okazawa, T. Toh, J. Fukuda, T. Kawase, M. Toki, Fluid flow in a continuous casting mold driven by linear induction motors, ISIJ Int. 41 (2001) 851–858, doi:10.2355/isijinternational.41.851.
[7] M. Dubke, K.H. Tacke, K.H. Spitzer, K. Schwerdtfeger, Flow fields in electromagnetic stirring of rectangular strands with linear inductors: Part I. theory and experiments with cold models, Metall. Trans. B 19 (1988) 581–593, doi:10.1007/BF02659149.
[8] M. Dubke, K.H. Tacke, K.H. Spitzer, K. Schwerdtfeger, Flow fields in electromagnetic stirring of rectangular strands with linear inductors: Part II. computation of flow fields in billets, blooms, and slabs of steel, Metall. Trans. B 19 (1988) 595–602, doi:10.1007/BF02659150.
[9] X. Wang, Y. Fautrelle, R. Moreau, J. Etay, A.M. Bianchi, F. Baltaretu, X. Na, Flow, heat and mass transfers during solidification under traveling/rotating magnetic field, Int. J. Energy Environ. Eng. 6 (2015) 367–373, doi:10.1007/s40095-015-0181-1.
[10] L. Hachani, R. Boussaa, B. Saadi, X. Wang, K. Zaidat, A. Belgacem-Bouzida, D. Henry, V. Botton, H. Ben Hadid, Y. Fautrelle, Experimental investigation of the natural and forced convection on solidification of Sn-3wt% Pb alloy using a benchmark experiment, J. Iron Steel Res. Int. 19 (2012) HAL Id : hal-00954379.
[11] D.J. Hebditch, J.D. Hunt, Observations of ingot macrosegregation on model systems, Metall. Mater. Trans. B 5 (1974) 1557–1564, doi:10.1007/BF02646326.
[12] G. Quillet, A. Ciobanas, P. Lehmann, Y. Fautrelle, A benchmark solidification experiment on an Sn-10%wtBi alloy, Int. J. Heat Mass Transf. 50 (2007) 654–666, doi:10.1016/j.ijheatmasstransfer.2006.07.030.
[13] X. Wang, P. Petitpas, C. Garnier, J.P. Paulin, Y. Fautrelle, A quasi two-dimensional benchmark experiment for the solidification of a tin-lead binary alloy, C. R. Mec. 335 (2007) 336–341, doi:10.1016/j.crme.2007.05.009.
[14] X. Wang, Y. Fautrelle, An investigation of the influence of natural convection on tin solidification using a quasi two-dimensional experimental benchmark, Int. J. Heat Mass Transf. 52 (2009) 5624–5633, doi:10.1016/j.ijheatmasstransfer.2009.05.030.
[15] L. Hachani, B. Saadi, X. Wang, A. Nouri, K. Zaidat, A. Belgacem-Bouzida, L. Ayouni-Derouiche, G. Raimondi, Y. Fautrelle, Experimental analysis of the solidification of Sn-3 wt.%Pb alloy under natural convection, Int. J. Heat Mass Transf. 55 (2012) 1986–1996, doi:10.1016/j.ijheatmasstransfer.2011.11.054.
[16] L. Hachani, K. Zaidat, B. Saadi, X. Wang, Y. Fautrelle, Solidification of Sn-Pb alloys: Experiments on the influence of the initial concentration, Int. J. Therm. Sci. 91 (2015) 34–48, doi:10.1016/j.ijthermalsci.2015.01.007.
[17] M. Bellet, H. Combeau, Y. Fautrelle, D. Gobin, M. Rady, E. Arquis, O. Budenkova, B. Dussoubs, Y. Duterrail, A. Kumar, C.A. Gandin, B. Goyeau, S. Mosbah, M. Založnik, Call for contributions to a numerical benchmark problem for 2D columnar solidification of binary alloys, Int. J. Therm. Sci. 48 (2009) 2013–2016, doi:10.1016/j.ijthermalsci.2009.07.024.
[18] A. Abdelhakem, L. Hachani, K. Zaidat, I. Sari, Y. Fautrelle, Experimental study of the effect of intermittent electromagnetic stirring on the columnar-equiaxed transition in Sn-10 wt % Pb alloy solidification, J. Heat Transfer. 143 (2021) 1–8, doi:10.1115/1.4050408.
[19] L. Hachani, J. Wang, I. Kaldre, G. Salloum Abou-Jaoude, O. Budenkova, G. Reinhart, K. Zaidat, N. Mangelinck, X. Li, H. Nguyen Thi, A. Bojarevics, Z. Ren, L. Buligins, Y. Fautrelle, Magnetic fields, convection and solidification, Mater. Sci. Forum. 790 (2014) 375–383, doi:10.4028/www.scientific.net/MSF.790-791.375.
[20] L. Hachani, K. Zaidat, Y. Fautrelle, Experimental study of the solidification of Sn-10 wt.%Pb alloy under different forced convection in benchmark experiment, Int. J. Heat Mass Transf. 85 (2015) 438–454, doi:10.1016/j.ijheatmasstransfer.2015.01.145.
[21] K. Zaidat, I. Sari, A. Boumaaza, A. Abdelhakem, L. Hachani, Y. Fautrelle, Experimental investigation of the effect of travelling magnetic field on the CET in Sn-10wt.%Pb alloy, IOP Conf. Ser. Mater. Sci. Eng. 424 (2018) 012052, doi:10.1088/1757-899X/424/1/012052.
[22] C.A. Gandin, T. Carozzani, H. Digonnet, S. Chen, G. Guillemot, Direct modeling of structures and segregations up to industrial casting scales, JOM 65 (2013) 1122–1130, doi:10.1007/s11837-013-0679-z.
[23] T. Carozzani, C.A. Gandin, H. Digonnet, M. Bellet, K. Zaidat, Y. Fautrelle, Direct simulation of a solidification benchmark experiment, Metall. Mater. Trans. A 44 (2013) 873–887, doi:10.1007/s11661-012-1465-1.
[24] J. Li, M. Wu, J. Hao, A. Ludwig, Simulation of channel segregation using a two-phase columnar solidification model - Part I: model description and verification, Comput. Mater. Sci. 55 (2012) 407–418, doi:10.1016/j.commatsci.2011.12.037.
[25] J. Li, M. Wu, J. Hao, A. Kharicha, A. Ludwig, Simulation of channel segregation using a two-phase columnar solidification model - Part II: Mechanism and parameter study, Comput. Mater. Sci. 55 (2012) 419–429, doi:10.1016/j.commatsci.2011.12.021.
[26] H. Combeau, M. Bellet, Y. Fautrelle, D. Gobin, E. Arquis, O. Budenkova, B. Dussoubs, Y. Duterrail, A. Kumar, S. Mosbah, T. Quatravaux, M. Rady, C.A. Gandin, B. Goyeau, M. Založnik, A numerical benchmark on the prediction of macrosegregation in binary alloys, in: Proceedings of the Supplemental Proceedings: Materials Fabrication, Properties, Characterization, and Modeling, 2, 2011, pp. 755–762, doi:10.1002/9781118062142.ch91.
[27] H. Combeau, M. Bellet, Y. Fautrelle, D. Gobin, E. Arquis, O. Budenkova, B. Dussoubs, Y. Du Terrail, A. Kumar, C.A. Gandin, B. Goyeau, S. Mosbah, T. Quatravaux, M. Rady, M. Založnik, Analysis of a numerical benchmark for columnar solidification of binary alloys, IOP Conf. Ser. Mater. Sci. Eng. 33 (2012) 012086, doi:10.1088/1757-899X/33/1/012086.
[28] S. Ganina, V. Ginkin, O. Budenkova, B. Saadi, L. Hachani, Y. Fautrelle, Comparison of two models for simulation of binary alloy solidification, Defect Diffus. Forum 326 (2012) 599–604, doi:10.4028/www.scientific.net/DDF.326-328.599.
[29] R. Boussaa, O. Budenkova, L. Hachaniu, X. Wang, B. Saadi, K. Zaidat, H. Ben Hadid, Y. Fautrelle, 2D and 3D numerical modeling of solidification benchmark of Sn-3Pb (%wt.) alloy under natural convection, CFD Model. Simul. Mater. Process. (2012) 163–170, doi:10.1002/9781118364697.ch19.
[30] K.O. Tveito, M. M'Hamdi, H. Combeau, M. Založnik, K. Zaidat, X. Wang, B. Saadi, Y. Fautrelle, Numerical analysis of the influence of melting and application of electromagnetic stirring prior to solidification on macrosegregation formation during casting of a binary alloy, CFD Model. Simul. Mater. (2012) 253–260, doi:10.1002/9781118364697.ch30.
[31] R. Boussaa, L. Hachani, O. Budenkova, V. Botton, D. Henry, K. Zaidat, H. Ben Hadid, Y. Fautrelle, Macrosegregations in Sn-3 wt%Pb alloy solidification: Experimental and 3D numerical simulation investigations, Int. J. Heat Mass Transf. 100 (2016) 680–690, doi:10.1016/j.ijheatmasstransfer.2016.04.120.
[32] A. Abdelhakem, A. Nouri, L. Hachani, Y. Fautrelle, K. Zaidat, Three-dimensional numerical simulation and experimental investigations of benchmark experiment of Sn-10 wt. %Pb alloy solidification under thermosolutal convection, J. Heat Transfer. 144 (2022) 042401, doi:10.1115/1.4053567.
[33] T. Wang, L. Hachani, Y. Fautrelle, Y. Delannoy, E. Wang, X. Wang, O. Budenkova, Numerical modeling of a benchmark experiment on equiaxed solidification of a Sn–Pb alloy with electromagnetic stirring and natural convection, Int. J. Heat Mass Transf. 151 (2020) 119414, doi:10.1016/j.ijheatmasstransfer.2020.119414.
[34] S. Khelfi, A. Abdelhakem, A. Nouri, L. Hachani, K. Zaidat, Numerical modeling and experimental analysis of benchmark experiment of Sn-10 wt%Pb alloy under forced convection by electromagnetic stirring, J. Cryst. Growth 584 (2022) 126575, doi:10.1016/j.jcrysgro.2022.126575.
[35] C. Wang, Z. Liu, B. Li, A three-phase volume-averaged solidification model considering the growth direction of columnar crystals axis, Int. J. Heat Mass Transf. 194 (2022) 122974, doi:10.1016/j.ijheatmasstransfer.2022.122974.
[36] Y. Zheng, M. Wu, E. Karimi-Sibaki, A. Kharicha, A. Ludwig, Use of a mixed columnar-equiaxed solidification model to analyse the formation of as-cast structure and macrosegregation in a Sn-10 wt% Pb benchmark experiment, Int. J. Heat Mass Transf. 122 (2018) 939–953, doi:10.1016/j.ijheatmasstransfer.2018.02.012.
[37] Z. Zhang, M. Wu, H. Zhang, E. Karimi-Sibaki, A. Ludwig, A. Kharicha, Modeling mixed columnar-equiaxed solidification of Sn- 10wt.%Pb alloy under forced convection driven by travelling magnetic stirring, IOP Conf. Ser. Mater. Sci. 861 (2020) 012024, doi:10.1088/1757-899X/861/1/012024.
[38] M. Wu, A. Ludwig, A three-phase model for mixed columnar-equiaxed solidification, Metall. Mater. Trans. A 37 (2006) 1613–1631, doi:10.1007/s11661-006-0104-0.
[39] M. Wu, A. Ludwig, Using a three-phase deterministic model for the columnar-to-equiaxed transition, Metall. Mater. Trans. A 38 (2007) 1465–1475, doi:10.1007/s11661-007-9175-9.
[40] J. Li, M. Wu, A. Ludwig, A. Kharicha, Simulation of macrosegregation in a 2.45-ton steel ingot using a three-phase mixed columnar-equiaxed model, Int. J. Heat Mass Transf. 72 (2014) 668–679, doi:10.1016/j.ijheatmasstransfer.2013.08.079.
[41] M. Wu, A. Ludwig, A. Kharicha, Volume-averaged modeling of multiphase flow phenomena during alloy solidification, Metals 9 (2019) 229, doi:10.3390/met9020229.
[42] J. Lipton, M.E. Glicksman, W. Kurz, Dendritic growth into undercooled alloy metals, Mater. Sci. Eng. 65 (1984) 57–63, doi:10.1016/0025-5416(84)90199-X.
[43] A. Ludwig, M. Wu, Modeling of globular equiaxed solidification with a two-phase approach, Metall. Mater. Trans. A 33 (2002) 3673–3683, doi:10.1007/s11661-002-0241-z.
[44] Y. Zheng, M. Wu, A. Kharicha, A. Ludwig, Incorporation of fragmentation into a volume average solidification model, Model. Simul. Mater. Sci. Eng. 26 (2018) 015004, doi:10.1088/1361-651X/aa86c5.

[45] H. Zhang, M. Wu, P. Schumacher, C.M.G. Rodrigues, A. Ludwig, A. Kharicha, Modelling melting and grain destruction phenomena during globular equiaxed solidification, Appl. Math. Model. 97 (2021) 821–838, doi:10.1016/j.apm.2021.04.024.
[46] Q. Han, A. Hellawell, Primary particle melting rates and equiaxed grain nucleation, Metall. Mater. Trans. B 28 (1997) 169–173, doi:10.1007/s11663-997-0139-7.
[47] J.P. Gu, C. Beckermann, A.F. Giamei, Motion and remelting of dendrite fragments during directional solidification of a nickel-base superalloy, Metall. Mater. Trans. A 28 (1997) 1533–1542, doi:10.1007/s11661-997-0215-2.
[48] B. Appolaire, H. Combeau, G. Lesoult, Modeling of equiaxed growth in multicomponent alloys accounting for convection and for the globular/dendritic morphological transition, Mater. Sci. Eng. A 487 (2008) 33–45, doi:10.1016/j.msea.2007.11.030.
[49] A. Kumar, M. Založnik, H. Combeau, G. Lesoult, A. Kumar, Channel segregation during columnar solidification: Relation between mushy zone instability and mush permeability, Int. J. Heat Mass Transf. 164 (2021) 120602, doi:10.1016/j.ijheatmasstransfer.2020.120602.
[50] M. Seredyński, J. Banaszek, Coupled enthalpy-porosity and front tracking approach to modeling chemical inhomogeneity in solidifying metal alloys, Int. J. Heat Mass Transf. 173 (2021) 121221, doi:10.1016/j.ijheatmasstransfer.2021.121221.
[51] A. Ludwig, M. Stefan-Kharicha, A. Kharicha, M. Wu, Massive formation of equiaxed crystals by avalanches of mushy zone segments, Metall. Mater. Trans. A 48 (2017) 2927–2931, doi:10.1007/s11661-017-4008-y.